Catalysis Today 282 (2017) 123–132

Contents lists available at ScienceDirect

Catalysis Today

journal homepage: www.elsevier.com/locate/cattod

# Vanadium and titanium oxide supported on mesoporous CMK-3 as new catalysts for oxidative desulfurization

Lorena Rivoira, Juliana Juárez, Horacio Falcón, Marcos Gómez Costa, Oscar Anunziata, Andrea Beltramone*

*Centro de Investigación en Nanociencia y Nanotecnología (NANOTEC), Facultad Regional Córdoba, Universidad Tecnológica Nacional, Maestro López y Cruz Roja Argentina, 5016, Córdoba, Argentina*

ARTICLE INFO

*Article history:*
Received 18 February 2016
Received in revised form 2 June 2016
Accepted 2 July 2016
Available online 7 July 2016

*Keywords:*
ODS
Ti-V supported CMK catalysts
Dibenzothiophenes
Ultra low sulfur diesel
Deactivation

ABSTRACT

Vanadium supported-CMK-3 catalysts with vanadium loading of 1–7 wt.% were studied in the oxidative desulfurization (ODS) of dibenzothiophene as a model sulfur compound. The activity was compared with titanium supported-CMK-3. Structural and textural characterization of the catalysts was performed by means of $N_2$ adsorption, XRD, UV–vis–DRS, Raman spectroscopy, XPS, TEM and TPR. The dispersion and the nature of the vanadium species depend on the V loading, so does the catalyst activity. Vanadium supported-CMK-3 with 7 wt.% of vanadium loading was the most active catalyst for ODS of DBT using hydrogen peroxide ($H_2O_2$) as oxidant and acetonitrile as solvent. 100% of DBT elimination was attained at short time in mild conditions. Carbon ordered mesoporous CMK-3 with high surface area and high pore volume promotes a very good anchorage of metallic oxides in the carbons framework reaching high active sites distribution and more stable nanoclusters. The reusability of the catalyst indicates that V-CMK-3 is a potential catalyst for the ODS of dibenzothiophene.



## 1. Introduction

Diesel emissions contribute to environmental issues associated to sulfur oxides released during the combustion process of fuels. Ultra-low-sulfur-diesel (ULSD) is diesel with substantially lowered sulfur content. Many countries have established regulations to restrict the S content in petroleum products to be 15 ppm and zero emission is even expected [1–4]. Dibenzothiophene derivatives are the predominant sulfur species remaining after hydrodesulfurization (HDS). This process is highly efficient for the removal of thiols, sulfides and disulfides, but it has low efficiency associated with the removal of refractory S-containing aromatic compounds especially the alkyldibenzothiophenes, because $H_2S$ produced during the reaction of some thiophene derivatives inhibited deep HDS of unreactive species. Furthermore, HDS process needs to be carried out at both high temperature and hydrogen pressure. To achieve the low-sulfur commercial fuel, alternative technologies have been introduced to overcome the present techniques [5–8]. Biodesulfurization [9] and adsorption [10,11] are new methods introduced to achieve ultra-low sulfur diesel. Unfortunately, both systems contribute more disadvantages wherein there are typically costly and causes excessive pollution. Alternatively, oxidative desulfurization (ODS) provides selective removal of those refractory sulfur compounds at proper temperatures and pressure and is capable to eliminate most refractory sulfur compounds in HDS [12]. That is how ODS is drawing significant research interest because of its simple processing and high efficiency [13–15]. This is the process wherein dibenzothiophene derivatives are converted to their corresponding sulfone. This approach is being actively pursued using a variety of different methodologies. Therefore, ODS has a great potential to become a complementary process to traditional HDS in the production of deeply desulfurized diesel fuels. Hence, liquid phase oxidation of sulfur compounds is the basis of the ODS process, since extraction step occurs rapidly and oxidation is the rate determining step [16]. By means of this procedure, in the presence of an oxidant and appropriate catalyst, sulfur containing compounds in diesel are converted in sulfoxide and/or sulfone which are easily separated from oil by liquid–liquid extraction with polar solvents or by adsorption [17,18]. Various oxidants such as *tert*-butyl hydroperoxide [19], hydrogen peroxide [13,14,20,21], ozone [22], etc. have been used for the oxidation of sulfur compounds. Among them, $H_2O_2$ has become a popular and the most widely used oxidant due to its availability and

* Corresponding author.
*E-mail addresses:* abeltramone@frc.utn.edu.ar, lelitajones@hotmail.com (A. Beltramone).

http://dx.doi.org/10.1016/j.cattod.2016.07.003
0920-5861/

environmentally benign properties [20,21]. In the field of catalysis, various acids [23–25], metallic ionic liquids (ILs) [26–29], homogeneous and heterogeneous polyoxometalate (POM) catalysts [30,31], and solid catalysts including activated carbon [32–34], titanium micro/mesoporous silica materials [20,35–39], homogeneous and heterogeneous rhenium catalyst [21], $VO_x/Al_2O_3$ [16], $WO_x/ZrO_2$ [40,41] and $Mo/Al_2O_3$ [42] have been used. Molecular sieves show good activity in the oxidation of different S-bearing compounds, and higher surface area materials such as V-MCM-41[35], Ti-modified SBA-15 [36], Ti-modified SBA-16 [20] and activated carbons [34] were also used as catalysts for the ODS.

Many attempts have been made to develop adsorbents for desulfurization of commercial fuels using metal-based porous materials such as zeolites, activated carbon and mesoporous silica. Mesoporous silicate materials are a suitable adsorbent due to their superior properties such as high surface area, tuneable and large pore size and high thermal stability which facilitate the diffusion of large molecules into the pores and overcome the pore-size limitation of zeolites [43]. Recently, we tested sulfur removal of different desulfurization systems; using several Ti modified mesoporous catalysts ($TiO_2$, $TiO_2$/SBA-16 and Ti-SBA-16) [20].

Mesoporous carbon materials are of interest in many applications because of their high surface area and physicochemical properties. With its well-ordered pore structure and tunable pore diameters in the mesopore range, ordered mesoporous carbon (OMC) is suitable for applications in catalysis. Mesostructured carbon CMK-3 has been obtained by template synthesis using SBA-15 mesostructured silicate. Our propose is to use a good sorbent material such as a mesoporous carbon as a support for the catalyst, functionalized with well known transition metals as active sites for ODS. There are a few reports in literature of the application of these materials as sorbents for S-compounds [44,45]. However, we have not found any report of mesoporous ordered carbon material as catalyst support applied in ODS process.

In this work we evaluate vanadium and titanium-based catalysts supported over a mesoporous carbon with large surface area (CMK-3) in the ODS of dibenzothiophene as a model sulfur compound.

## 2. Experimental

### 2.1. Synthesis of the catalysts

#### 2.1.1. Materials

Tetraethylorthosilicate (TEOS, 98%, Sigma–Aldrich), Poly(ethylene glycol)-block-poly(propylene glycol)-block-poly (ethylene glycol), ($EO_{20}PO_{70}EO_{20}$, P123-Sigma–Aldrich), Sucrose (≥99.0%, FLUKA), Vanadium(III) chloride (99.999%, Sigma–Aldrich). Tetrabutylortotitanate (TBOT, 99.0%, Sigma–Aldrich).

#### 2.1.2. Synthesis of Si-SBA-15

SBA-15 was used as the template in the synthesis of CMK-3. The synthesis of the ordered mesoporous silica SBA-15 was prepared according to a previous work [46]. Typically, 20 g of P123 (Poly(ethylene glycol)-block-poly(propylene glycol)-block-poly (ethylene glycol)) was dissolved at 50 °C in 1 M HCl solution. Then, 40 g of TEOS were added and the resulting mixture was stirred at 50 °C for 24 h. The milky mixture was transferred into a Polypropylene bottle and it was kept at 100 °C for 72 h. The solid was filtered, washed with deionized water until pH ~6. The molar composition was Si: 0.018 $EO_{20}PO_{70}EO_{20}$: 2.08 HCl: 112 $H_2O$. To extract the template, the material was first immersed in ethanol reflux for 6 h. Then, the product was filtered, washed, and dried in air at 90 °C. To ensure the elimination of the structure-directing agent, the sample was heated under $N_2$ flow of 20 mL/min at 300 °C and then a calcined at 550 °C in air for 6 h.

#### 2.1.3. Synthesis of CMK-3 carbon

The synthesis of CMK-3 mesoporous carbon was carried out using SBA-15 as the hard template and sucrose as the carbon precursor, following the synthesis procedure described in our previous work [46]. Briefly 1.1 g of sucrose was dissolved in a solution of $H_2SO_4$ (0.14 g) in water (5 g). 1 g of SBA-15 was added to the solution. The resulting mixture was dried at 100 °C and then was heated up and kept at 160 °C for 6 h. A second impregnation was performed in order to ensure the filling of the template pores with the carbon precursor, using an $H_2SO_4$ solution with 0.75 g of sucrose. The mixture was dried at 100 °C and heated up and kept at160 °C for 6 h. Then, the brown powder obtained was heated up to 900 °C under nitrogen flow (20 mL/min).

The silica removal was performed using a HF solution (5 wt.%) at room temperature. The carbon sample was filtered, washed with ethanol solution and dried at 120 °C.

#### 2.1.4. Synthesis of V-CMK-3 and Ti-CMK-3

Vanadium was incorporated into the ordered mesoporous carbon CMK-3 by wetness impregnation using $VCl_3$ as the source of Vanadium. The metal precursor ($VCl_3$) was dissolved in 20 mL of ethanol under vigorous stirring.The solution was placed in a rotary evaporator to remove excess of ethanol at about 50 °C and 50 rpm. The obtained powder was then dried at 100 °C, overnight. The dried process of the V-CMK-3 samples at 100 °C in a furnace in presence of air is sufficient to oxidize the vanadium species to vanadium pentoxide and prevent the carbon combustion. Then, the resulting material was heated in a dynamic inert atmosphere (nitrogen flow of 20 mL/min) from 25 to 200 °C with a slope of 4 °C/min and then, the temperature was increased to 470 °C with a slope of 10 °C/min and kept at this temperature during 5 h. Samples with different load of vanadium were prepared. The samples were named V-CMK-3 (1, 3 and 7 wt.%).

Similarly, titanium was incorporated into the ordered mesoporous carbon CMK-3 by wetness impregnation using Tetrabutylortotitanate (TBOT) as the source of titanium. The metal precursor (TBOT) was dissolved in 10 mL of ethanol under vigorous stirring, in order to have a nominal content of 7 wt.% of Ti in the final solid. CMK-3 was incorporated to the solution and placed in a rotary evaporator to remove excess of ethanol at about 40 °C and 60 rpm. The powder obtained was then dried at 100 °C, overnight. Finally, the resulting material was heated in a dynamic inert atmosphere (nitrogen flow of 20 mL/min) from 25 to 200 °C with a slope of 4 °C/min and then the temperature was increased to 470 °C with a slope of 10 °C/min and kept at this temperature during 5 h. The sample was named Ti-CMK-3.

### 2.2. Characterization of the catalysts

XRD patterns were collected by using a continuous scan mode.The scan speed was 0.02° (2θ)/min in the Philips X'Pert PRO PANalytical diffractometer, operating with CuKa X-ray radiation (X-ray generator current and voltage set at 40 mA and 45 kV), using small divergence and scattering slits of 1/32 mm and a goniometer speed of 1.2° (2θ) $min^{-1}$. The scanning range was set between 0.5° and 5°. The sample was crushed previously and placed in an aluminum sample holder. Elemental analysis was performed by inductively coupled plasma-atomic emission spectroscopy (VISTA-MPX) operated with high frequency emission power of 1.5 kW and plasma airflow of 12.0 L/min. TPR was performed using a Micromeritics Chemisorb 2720 apparatus, with a flow of 14 mL/min of 10 mol% of $H_2/N_2$ heating up 500 °C, with a preheating treatment at 380 °C in an inert atmosphere ($N_2$). $N_2$ adsorption/desorption isotherms at 77 K were measured on ASAP 2020 equipment after degassing the samples at 673 K, determining textural properties as surface area and pore volume; pore size distribution was estimated

using Barrett, Joyner, and Halenda algorithm. Ultraviolet-visible diffuse reflectance spectroscopy (UV–vis-DRS) were recorded with a Perkin Elmer Lamba 650 spectrophotometer equipped with a diffuse reflectance accessory. Raman spectrum was obtained from an InVia Reflex Raman microscope and spectrometer using a 532 nm diode laser excitation. X-ray Photoelectron Spectra (XPS) were obtained on a MicrotechMultilb3000 spectrometer, equipped with a hemispherical electron analyzer and MgKα ($h\nu = 1253.6$ eV) photon source. An estimated error of ±0.1 eV can be assumed for all measurements. Peak intensity was calculated from the respective peak areas after background subtraction and spectrum fitting by a combination of Gaussian/Lorentzian functions. TEM were recorded in a JEOL 2100F microscope operated with an accelerating voltage of 200 kV (point resolution of 0.19 nm); coupled with Energy dispersive X-ray spectroscopy (EDS).

### 2.3. Catalytic activity

The catalytic oxidation of DBT with hydrogen peroxide was carried out in a glass batch reactor, equipped with a magnetic stirrer, a thermometer and a condenser. In a typical run, the solid catalyst (60 mg) was suspended under stirring (750 rpm) in 20 mL of a solution of 500 ppm of S as DBT in acetonitrile. Then, appropriate amount of 30% aqueous $H_2O_2$ was added at constant temperature (60 °C). Most of the experiments were performed in a two-phase liquid-solid (L (solvent) −S (catalyst)) system, where acetonitrile was used as solvent. When the experiments were performed in a three-phase liquid-liquid-solid (L (oil) −L (solvent) −S (catalyst)) system, acetonitrile was used as solvent and dodecane as oil phase.

Solution samples were recovered at various times. The products were analyzed by GC HP 5890 Series II with a HP-5 column and connected to FID and PFPD detectors, after filtration and eventually decantation step. The products were confirmed using a Shimadzu GCMS-QP5000 with a GC-17A gas chromatograph and AOC-20i autoinjector and HP-5 column 30-m length, 25-mm inner diameter, and 25-μm film thickness.

## 3. Results and discussion

### 3.1. Characterization of the catalysts

#### 3.1.1. XRD

Low angle X-ray diffraction patterns for CMK-3, V-CMK-3 and Ti-CMK-3 are shown in Fig. 1. In the case of the mesoporous carbon CMK-3, obtained by hard templating of SBA-15, the pattern indicates that the carbon CMK-3 is an exact replica of the template, indicated by the appearance of peaks consistent with the symmetry of SBA-15 [47].

In the case of the modified catalysts with vanadium and titanium, the overall pore structure is maintained as indicated by the appearance of low-angle diffraction peaks. However, the intensity of the main peak [110] decrease in both cases compared to the pristine CMK-3. This decrease might be due to the reduction of scattering contrast induced by the dispersed nanoparticles [48].

Fig. 2 shows the wide-angle XRD patterns of the pristine CMK-3 (inset) and the modified catalysts Ti-CMK-3 and V-CMK-3. It can be observed that the CMK-3 presents two broad peaks indexed to the planes [002] and [100] typical for graphite carbons [46].

No diffraction peaks corresponding to vanadium oxides were detected in V-CMK-3 catalysts, indicating that VOx species are highly dispersed on the CMK-3 surface [49].

The pattern of Ti-CMK-3 shows characteristic signals of $TiO_2$ in anatase phase [50], indicating that the incorporation of titanium as anatase was successful. The absence of prominent reflections in $TiO_2$ clusters indicates that no crystalline bulk material has been formed [51]. $TiO_2$ nanoparticles were formed with nanometric size and high dispersion (very broad XRD $TiO_2$ signals). This can be ascribed to a relatively low scattering contrast between the pores and walls of mesoporous materials, due to the formation of anatase nanoclusters with a narrow size distribution [52]. Table 1 shows the XRD parameters of the samples, in the case of V-CMK-3 we observe that $a_0$ decreases as the vanadium loading increases, this indicates

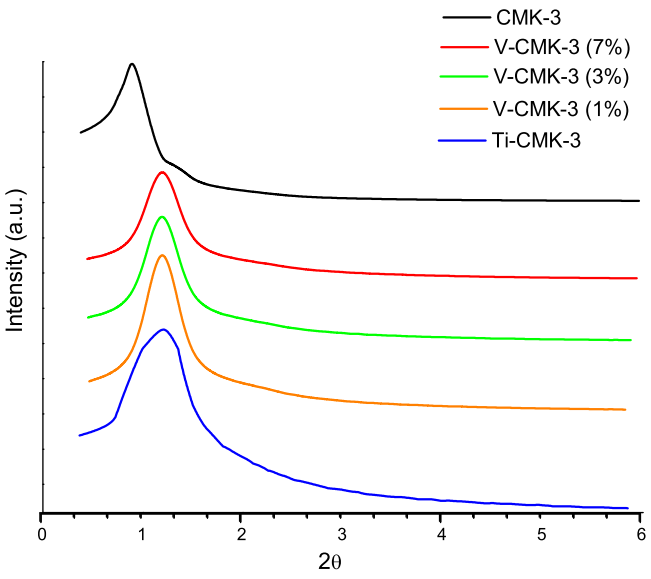


**Fig. 1.** Small-angle XRD patterns of the samples.

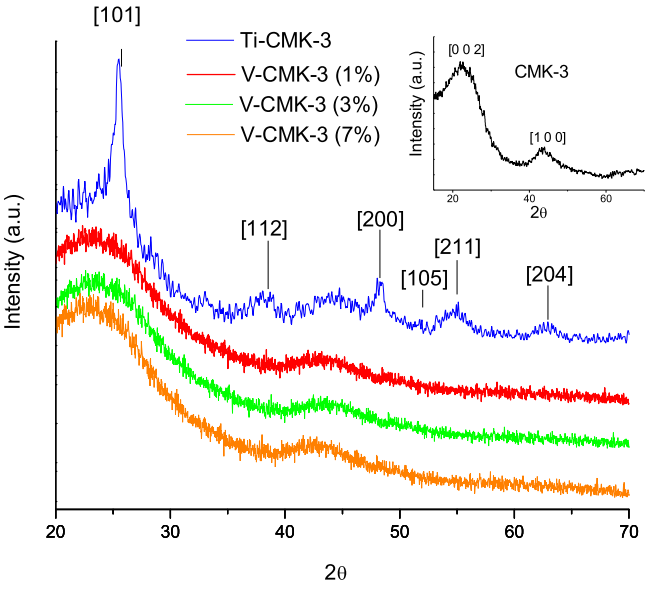


**Fig. 2.** Wide-angle XRD patterns of the samples; CMK-3 (Inset).

**Table 1**
XRD parameters of the samples.

| Sample | SBA-15 [*hkl*] | | | CMK-3 [*hkl*] | | | $a_o$ (nm) |
|---|---|---|---|---|---|---|---|
| | [100] d (nm) | [110] | [200] | [100] d (nm) | [110] | [200] | |
| SBA-15 | 8.6 | 5.0 | 4.3 | – | – | – | 10.0 |
| CMK-3 | – | – | – | 10.5 | 6.1 | 5.2 | 12.1 |
| Ti-CMK-3(7%) | – | – | – | 7.1 | 4.4 | 3.8 | 8.6 |
| V-CMK-3(1%) | – | – | – | 7.2 | 4.2 | 3.9 | 8.5 |
| V-CMK-3(3%) | – | – | – | 7.1 | 4.2 | 3.7 | 8.3 |
| V-CMK-3(7%) | – | – | – | 7.0 | 4.1 | 3.5 | 8.1 |

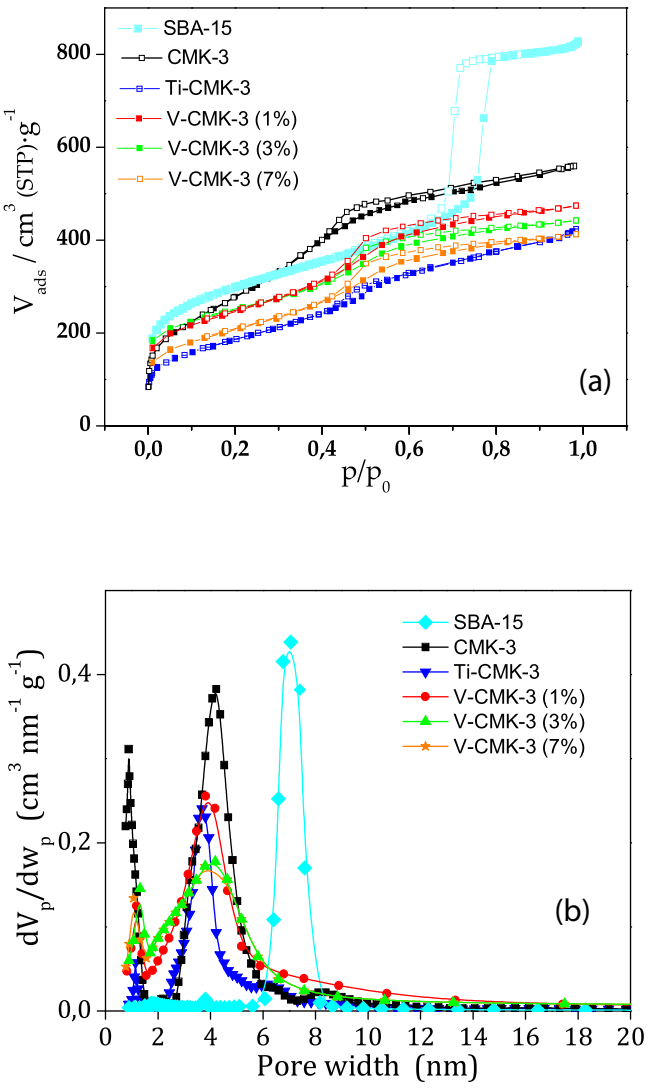


**Fig. 3.** (a) Nitrogen adsorption (solid symbols)–desorption isotherm (open symbols) at 77 K and (b) pore size distribution of the samples.

the direct anchoring of the metal through the surface oxygen groups of the pristine support.

### 3.1.2. Adsorption/desorption isotherms analysis

Fig. 3a shows the $N_2$ adsorption/desorption isotherms for SBA-15, CMK-3, V-CMK-3 and Ti-CMK-3 samples at 77 K. The nitrogen adsorption/desorption isotherms for CMK-3, V-CMK-3 and Ti-CMK-3 are typical type IV curves exhibiting hysteresis loops type H2, according to IUPAC classification, typical of mesoporous solids. The materials obtained exhibit capillary condensation to relative pressures about 0.40 and 0.45, which can be related to the pore blocking effect of influencing pressure where evaporation/desorption pore occurs. The increase in adsorption at a low relative pressure is associated with the presence of micropores or a strong adsorbate-adsorbent interaction. Mesoporous carbons exhibit microporosity in the nanochannel walls; therefore, CMK-3 presents higher surface area than SBA-15, but lower Vp and Wp, because volume and wide size correspond only to the mesoporous. The pore size distribution of CMK-3 shows a sharp peak at 4.5 nm indicating a quite regular array of nanopores. To demonstrate the presence of microporosity, we show the pore size distribution under 1.8 nm (Fig. 3b). The length of inflection shortens gradually with increasing V loading in V-CMK-3 samples, corresponding to a reduction in the volume and

**Table 2**
Textural properties of the samples.

| Material | $S_{BET}$ ($m^2$ $g^{-1}$) | $V_{\mu P}$ ($cm^3$ $g^{-1}$) | $V_{TP}$ ($cm^3$ $g^{-1}$) | $W_p$ (nm) |
|---|---|---|---|---|
| SBA-15 | 1040 | 0.57 | 1.38 | 7 |
| CMK-3 | 1323 | 0.23 | 1.01 | 4.5 |
| V-CMK-3 (1%) | 1176 | 0.15 | 0.84 | 3.9 |
| V-CMK-3 (3%) | 1035 | 0.13 | 0.83 | 3.8 |
| V-CMK-3 (7%) | 847 | 0.11 | 0.80 | 3.7 |
| Ti-CMK-3 (7%) | 775 | 0.10 | 0.75 | 3.6 |

$V_{TP}$: Total pore volume; $S_{BET}$: BET surface area.
$V_{\mu P}$: Micropore volume; $W_P$: Wide mesopore.

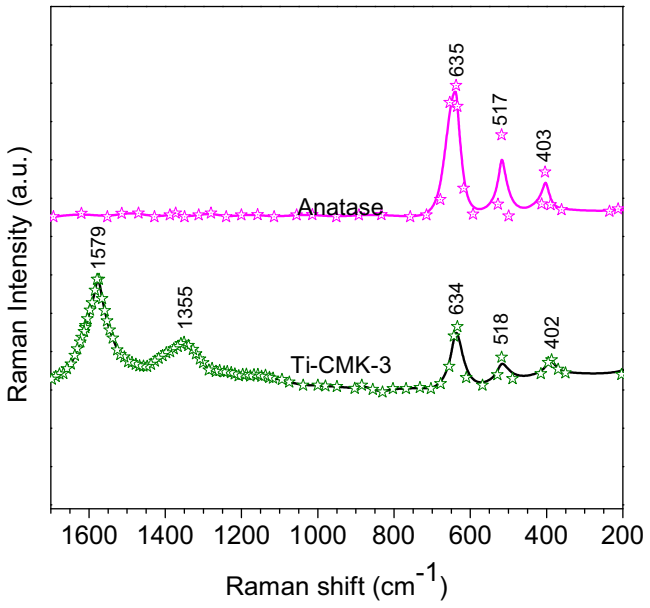


**Fig. 4.** Raman spectra of Ti-CMK-3 and pure anatase.

size of the pore (see Table 2). The small shift to a lower pore diameter upon vanadium loading reflects the formation of nanoparticles inside the mesopores of CMK-3. Pore size distribution of Ti-CMK-3 show a broad peak with a maximum at approximately 3.6 nm, which corresponds to primary mesopores. In the case of the high loaded samples we observe a decreasing in the surface area, compared with pure CMK-3, due to the load of channels because of the oxide nanoparticles. Considering that large bulk of vanadia crystallites are not formed in the V-CMK-3 samples, the decrease in the surface area is not remarkable.

### 3.1.3. Raman studies

Fig. 4 shows the Raman spectra of Ti-CMK-3 and pure anatase in the range of 200–1700 $cm^{-1}$. The characteristic signals of anatase were detected in the Ti-CMK-3 sample [53]. The typical absorption of CMK-3 also can be seen in Ti-CMK-3 sample. The peak at 1355 $cm^{-1}$ is associated with vibrations of C—C bond, referred to D band, attributed to the configuration of disordered graphite [54,55]. This band also could be ascribed to a diamond-like atomic arrangement in the graphite samples, probably as partially tetrahedrally bonded. The peak at 1579 $cm^{-1}$ is called G band, correspond to an E2 g mode of graphite, related to C=C-double bonded carbon vibration in hexagonal lattice [56,57]. It could be clearly seen that G and D band intensity of Ti-CMK-3 was not perturbed significantly.

### 3.1.4. XPS

Fig. 5 shows the binding energy of V2p$_{3/2}$ core level in V-CMK-3 samples. The only contribution observed for all the samples at 517.0-517.2 eV is assigned to $V^{5+}$ in the form of $V_2O_5$. The contri-

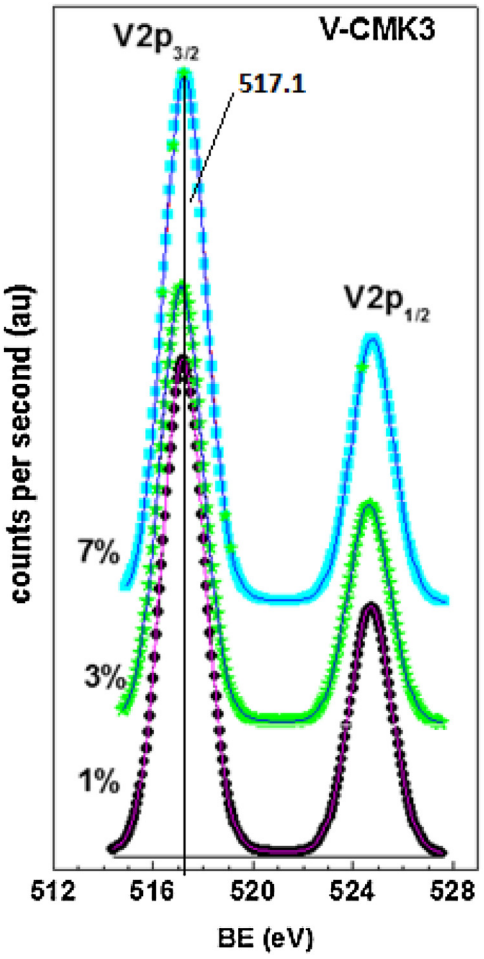


**Fig. 5.** XPS of V-CMK-3 samples.

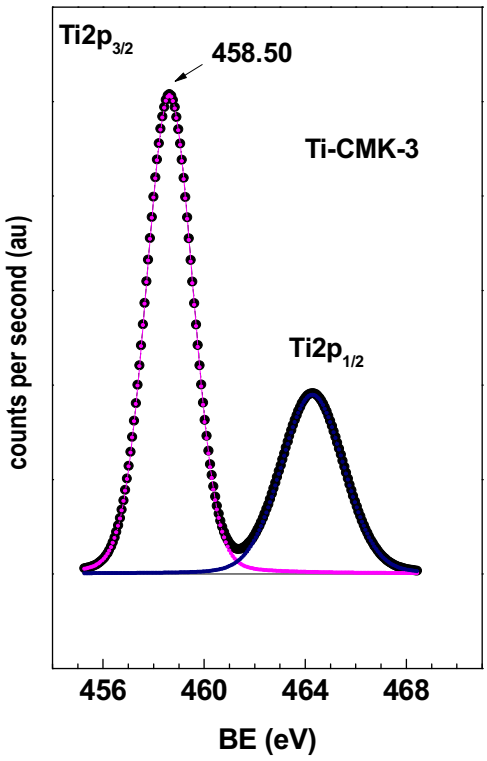


**Fig. 6.** XPS of Ti-CMK-3.

bution centered about 516.3 eV attributed to $V^{4+}$ species was not observed [58,59]. O1 s core level spectrum (not showed) presents a contribution located about 531–532 eV, typical for $V_2O_5$ [60]. The second contribution is a shoulder of the first contribution centered about 532.7–533 eV attributed to the oxygen associated with chemisorbed water (expressed as O'α) [58,59]. The atomic ratio of V/C (at 50–100 Å of deep) was 0.007, 0.020, 0.035 (around 0.33, 0.81 and 1.5 wt.%) for V-CMK-3(1%), V-CMK-3(3%) and V-CMK-3(7%), respectively. Whereas for EDS studies the nominal V content was 1.02, 2.98 and 7.01 wt.%, respectively. This indicates that most of the particles are in the porous and channels of CMK-3 material as small $V_2O_5$ nanocrystals.

Analysis of Ti species also was performed by XPS; the results are shown in Fig. 6. According literature [61] $TiO_2$ as anatase, can be easily determined by XPS following $Ti2p_{3/2}$ at 458.6 eV BE. The presence of this band in Ti-CMK-3 demonstrated that Ti is incorporated in anatase phase. The atomic ratio of Ti/C was 0.038 (around 1.8 wt.%) for Ti-CMK-3. The nominal Ti content was 6.897 wt.% determined by EDX. Ti species are also located mostly in the channel/pore of the support.

### 3.1.5. TEM

Fig. 7A shows TEM images of CMK-3. The image reveals particles of the nanometric carbon consisting of many rope-like domains (rod-like particles) with relatively uniform sizes of about 1 μm long and 0.2 wide. TEM image of V-CMK-3 (7%) is shown in Fig. 7B. Vanadium oxide nanoclusters were not seen probably due to a low contrast in the TEM image. TEM images for Ti-CMK-3 (Fig. 7C and D) show an ordered structure slightly damaged by thermal treatments; they also exhibit well-organized pores parallel to each other. In Fig. 7C and D a dark spot indicates anatase nanoclusters. Particle size distribution ranged from 1 to 11 nm and mean particle diameter was found to be close to 5 nm, indicating that most of the particles reside within of the pore system.

### 3.1.6. UV–vis–DRS

UV–vis diffuse reflectance spectroscopy (UV–vis–DRS) was used to study the dispersion and chemical environment of the metal incorporated in the carbon material. Fig. 8 shows the UV–vis–DRS spectrum of the synthesized samples. The bands at 210, 240–320 and 320–400 nm, correspond to isolated framework Ti (IV), octahedral coordinated Ti species, and titania (anatase) phase, respectively [62–64]. In the Ti-CMK-3 sample, the presence of an absorption band in the range of 240–320 nm suggests that Ti ions occupy sites characteristic of extra-framework titanium corresponding to octahedral coordinated Ti species in anatase phase. The intense ligand-to-metal charge transfer transition band at ~210 nm attributed to mono-atomically dispersed $Ti^{4+}$ ions in tetra-coordinated geometry, is not present in the sample [62]. The absence of the absorption band at higher wavelength range, indicates that the size of the pore channels of CMK-3 avoid the growing of the $TiO_2$ particles, obtaining a very small size of the crystal of anatase.

Fig. 8, also shows the UV–vis–DRS spectra of V-CMK-3 samples. A decrease of the energy with increasing vanadium content is identified, reflecting an increase in the size and dimensionality of VO*x* domains as vanadium surface density increases [65,66]. The catalysts with lower load of vanadium show a ligand to a metal charge transfer (LMCT) band at 260–270 nm due to electronic transitions of $O^{2-}$ to $V^{5+}$ which can be assigned to tetrahedral $V^{5+}$ species [67–69]. This band shifts to higher wavelength as V loading increases. It has been reported [70] that the band maximum of the CT transitions of $V^{5+}$ shifts to higher wavelength with increasing coordination num-

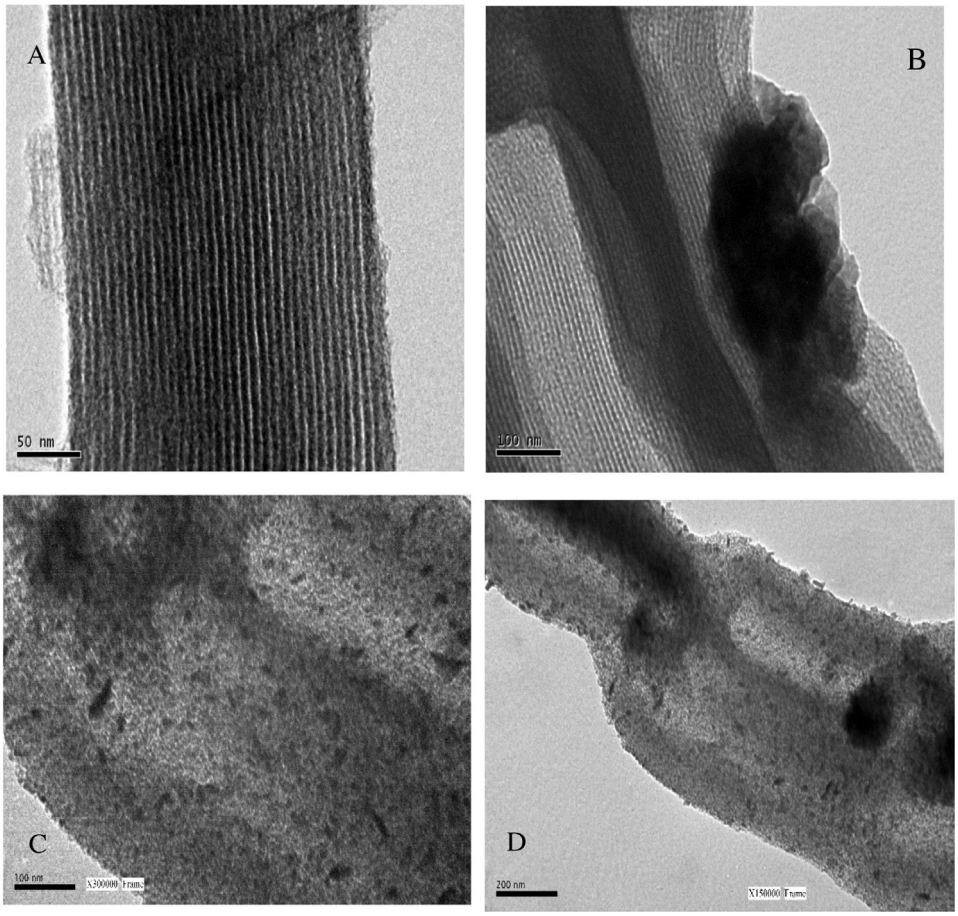


**Fig. 7.** TEM Images (A) CMK-3; (B) V-CMK-3; (C and D) Ti-CMK-3.

ber and that the polymerization of tetrahedral $V^{5+}$ is only evidenced by a broadening of the absorption bands and/or a small shift of the absorption maxima to lower energy (higher wavelength).

In addition, a new feature at 340–500 nm appears for all samples, pointing to the presence of "bulk-like" $V_2O_5$ crystallites due to a further polymerization of the V species [71–75]. Thus, the present observation of the increase of the relative intensities of the absorptions at 340–500 nm with increasing vanadium content can be attributed to the presence of vanadium species with a larger polymerization degree in the highest loaded sample. The band of bulk $V_2O_5$ (ca. 450 nm) is not detected, and nanocrystalline vanadia is most probably present, as indicated by XRD. These results indicate that these catalysts present a heterogeneous surface composed of tetrahedral vanadate species and possibly segregated octahedral $V_2O_5$-like species, especially in the V-CMK-3 (7%).

### 3.1.7. TPR

To investigate the reducibility of vanadium species dispersed on the support, the $H_2$–TPR profiles of the catalysts are comparatively depicted in Fig. 9.

There is one reduction peak for all catalysts, assigned to the reduction of $V^{5+}$ [76–81]. The peak temperature centered at 604 °C is observed on the sample with lowest V loading attributed to the reduction of dispersed tetrahedral vanadium species or low oligomeric V–O–V groups. For V-CMK-3(7%) sample, the peak is shifted to higher temperature of 630 °C, suggesting that the formation of $V_2O_5$-like polymeric vanadium species at high vanadium loading will slightly retard the reduction of $V^{5+}$.

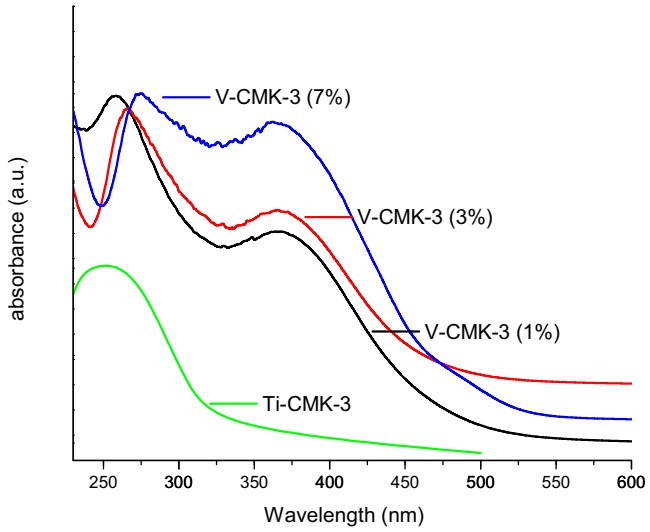


**Fig. 8.** UV–vis–DRS of the samples.

## 3.2. Catalytic activity

We tested sulfur removal of different desulfurization systems. In first instance we investigated the adsorption process, when bare mesoporous CMK-3 sample was used as the adsorbent for desulfurization from model feed. These studies were carried out using

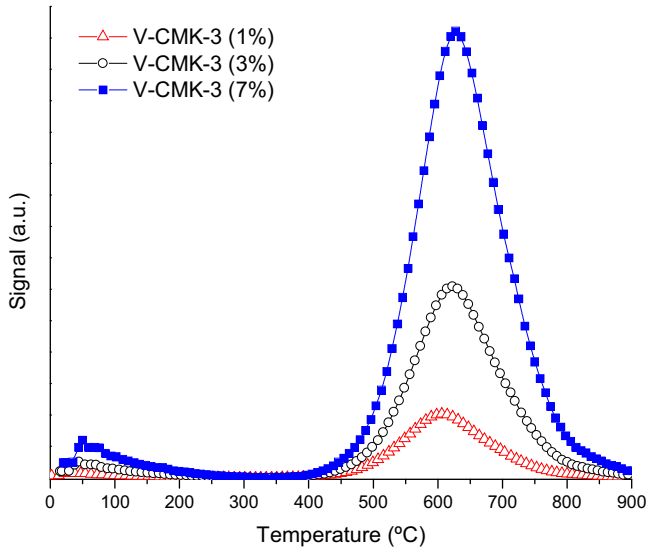


**Fig. 9.** TPR of the V-CMK-3 samples.

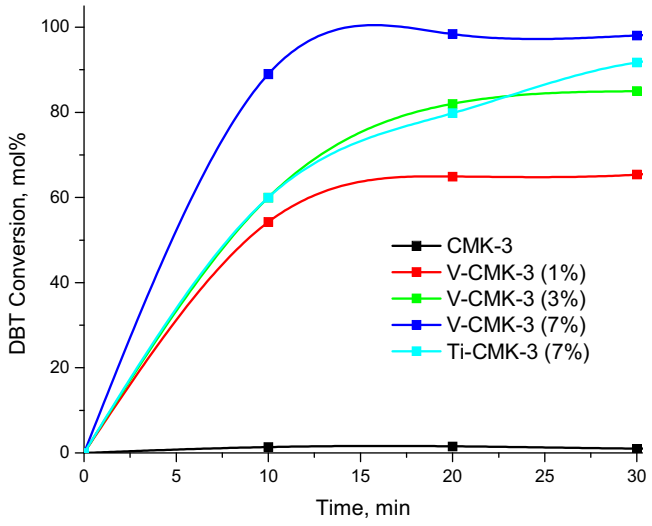


**Fig. 10.** Catalytic activity of the samples. Molar ratio O/S = 12, T = 60 °C. g DBT/g cat = 1.2 (500 ppm).

three different DBT initial concentrations and 60 mg of the adsorbent (CMK-3) at 25 °C for 60 min. The amount of DBT adsorbed was dependent on the initial DBT concentration. The adsorption amount increased from 8.52 wt.% to 17 wt.% when the initial concentration of DBT increased from 250 to 500 ppm. However, higher initial DBT concentration (1000 ppm) shows a lower adsorption amount (6.12 wt.%) of DBT. The effect of temperature on the adsorption of DBT onto CMK-3 was investigated by the same process at different temperatures in a water bath. The results indicated that the equilibrium adsorption amount of DBT decreases by increasing temperature, in agreement with literature [44].

No conversion of DBT in presence of $H_2O_2$ ($H_2O_2$/S = 6) was obtained at 60 °C in the absence of the catalyst. This result indicated that the blank experiment without catalyst and with pure support (CMK-3) show no conversion and the V-Ti-oxide species present in CMK-3 play the main role in the catalytic activity (Fig. 10).

Fig. 10 shows the catalytic results from the ODS of DBT using the different synthesized catalysts in a liquid-solid (L–S) phase system. Acetonitrile was used as solvent for the liquid phase. DBT was oxidized to it sulfone (100% yields); sulfoxide or other products were not detected in the conditions studied. From the Figure, we

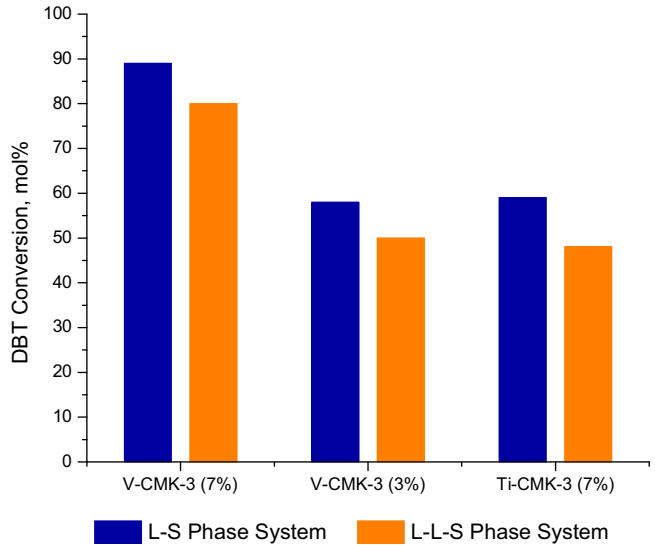


**Fig. 11.** DBT conversion in L–S phase system (acetonitrile as polar phase) and in L–L–S phases system (acetonitrile as polar phase and dodecane as oil phase). Molar ratio O/S = 12, g DBT/g cat = 1.2 (500 ppm), T = 60 °C. Reaction time = 10 min.

can note that at 15 min of reaction time, V-CMK-3 (7%) displays a DBT conversion of almost 100%. The samples with less content of V showed lower activity. Also the titanium modified sample Ti-CMK-3 was less active than the vanadium sample with the same loading. Vanadium oxides were more active than titanium oxide in this condition. CMK-3 was inactive for this reaction. In the case of the vanadium samples with lower V-content, we observe a maximum in conversion and then it remains constant, this fact can be explain in terms of the oxidized reaction products might reside on the catalyst surface, blocking the adsorption sites where reactive oxygen species are formed. K. Cho et al. [82], observed that the overall ODS activity using Ti-SBA-15, was drastically decreased due to the competitive oxidation and the deposit of the oxidized S compounds on the catalyst surface, poisoning the adsorption sites.

In the case of V-CMK-3, the higher activity of the more loaded sample could be explained in terms of the number of active sites exposed. The superior DBT desulfurization of this material suggests a determining effect on $VO_x$ species critical size, with greater exposed surface area.

The effect of mass transfer was studied comparing two different phase systems. Fig. 11 shows the catalytic results from the ODS of DBT using the most active catalysts in a liquid-solid (L–S) phase system and in a three-phase liquid-liquid-solid (L (oil) –L (solvent) –S (catalyst)) system, where the proposed mechanism for the catalytic oxidation of DBT in the reaction occurs by simultaneous extraction/oxidation of dibenzothiophene in acetonitrile solution, wherein is the catalyst and $H_2O_2$. The surface sites in the catalysts are capable of interacting with $H_2O_2$ to produce large amounts of superoxide radical. These radical species can oxidize the DBT molecules in acetonitrile phase to their corresponding sulfones and hence polar sulfones do not migrate into the oil phase. The catalytic cycle can take place multiple times under low $H_2O_2$ concentration and low temperature conditions. If the liquid–liquid extraction step does not occur rapidly, the transfer of DBTs from the oil phase to the solvent phase will affect the rate of the global process. Fig. 11 shows slight higher conversions of all catalysts in the L-S phase system, probing the existence of mass transfer limitation.

Therefore, in the subsequent experiments we will use a two phase-system.

Thus, DBT concentrations ranging from 500 ppm to 2000 ppm were selected while maintaining the other variables constant.

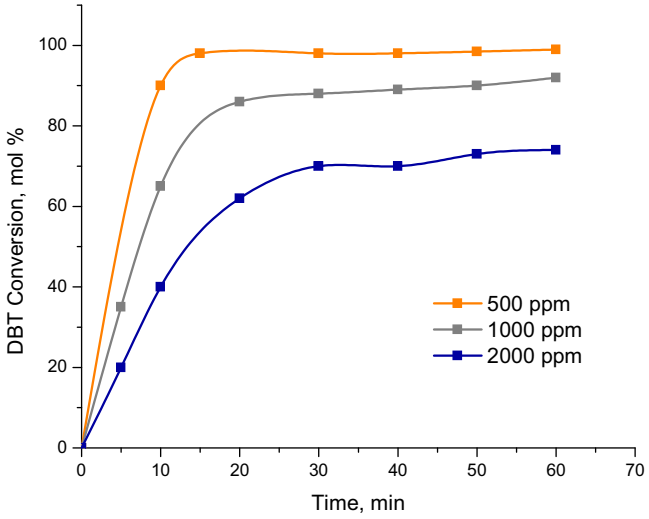


**Fig. 12.** Effect of the initial concentration of DBT over V-CMK-3 (7%). Molar ratio O/S = 12, T = 60 °C. Cat = 60 mg, in L–S phase system.

Fig. 12 shows DBT conversion as a function of the reaction time for different initial DBT concentrations using our best catalyst. Higher conversion is obtained with low DBT initial concentrations as is expected [14,26,83,84].

D. Huang et al. [84] studied the DBT conversion as a function of the reaction time for different DBT concentrations. They found that reaction rate with low DBT initial concentration was much higher than that of a higher concentration. This behavior was explained as the molar ratio of $H_2O_2$ to DBT is an important factor in the DBT oxidation, for the lowest DBT concentration was much higher than for the reaction with high DBT concentration. On the other hand, DBT was oxidized to the corresponding DBT sulfones, which are more polar than DBT. The sulfones adsorb onto the surface of the catalyst, leading to fewer active sites which have access to the reactant during oxidation.

Y. Nie et al. [26] showed the effect of initial S-content on S-removal. They found that S-removal increased as initial sulfur concentration decreased from1000 ppm to 500 ppm at 50 °C. However, S-removal slightly decreased as initial S-content decreased from 1000 ppm to 500 ppm at 25 °C. This result further states that initial S-content is a key factor affecting S-removal at the high temperature. Jia et al. [14] studied the oxidative removal of DBT at different sulfur concentrations. The lower the concentration was, the faster the removal rate of DBT. They assumed that the competition of adsorption between DBT and the oxidized products on the catalyst under relative high sulfur concentration resulted in the decrease of the DBT oxidation rate.

However, very high conversion at short times was obtained with V-CMK-3. This fact demonstrates the efficiency of this catalyst in this process.

The influence of hydrogen peroxide concentration on the conversion of DBT was explored. Different $H_2O_2$/DBT molar ratios were selected (Fig. 13). In the stoichiometry of this reaction, only 2 mol of $H_2O_2$ are consumed per mole of sulfone (R-$SO_2$) produced. However, the reaction rate increases as the $H_2O_2$/DBT ratio increases; the reaction rate is the highest for $H_2O_2$/DBT = 10/1 molar ratio (O/S = 20), for which complete DBT conversion was achieved at 60 min (note that we are using a very high initial concentration of S). The reaction is favored under excess of hydrogen peroxide. Although the reaction rate is slightly lower with $H_2O_2$/DBT = 6/1 molar ratio, 70% of DBT conversion can be reached at 60 min. In resume, V-CMK-3 is capable to eliminate 100% of sulfur of high concentrated sulfur-model diesel in the adequate conditions and short times.

Vanadium and titanium oxide supported CMK-3 had an excellent performance in the conditions tested. They also have demonstrated to be more active than Ti-supported silica mesoporous SBA-16 studied in our previous work [20]. Several studies on oxidation of benzothiophene, in similar conditions that used in this work, were reported in literature. ODS of benzothiophene showed good results over different Ti-containing molecular sieves [85], Ti-SBA-15 catalyst [86] and Ti-Beta and Ti-MCM-41 catalyst using different oxidants [87]. Cedeño-Caero et al. [88–90] applied different vanadium catalyst on the oxidative desulfurization of model diesel obtaining good performance. However, the comparison with the results reported here makes V-CMK-3 a very promising catalysts for the ODS of sulfur compounds present in fuels.

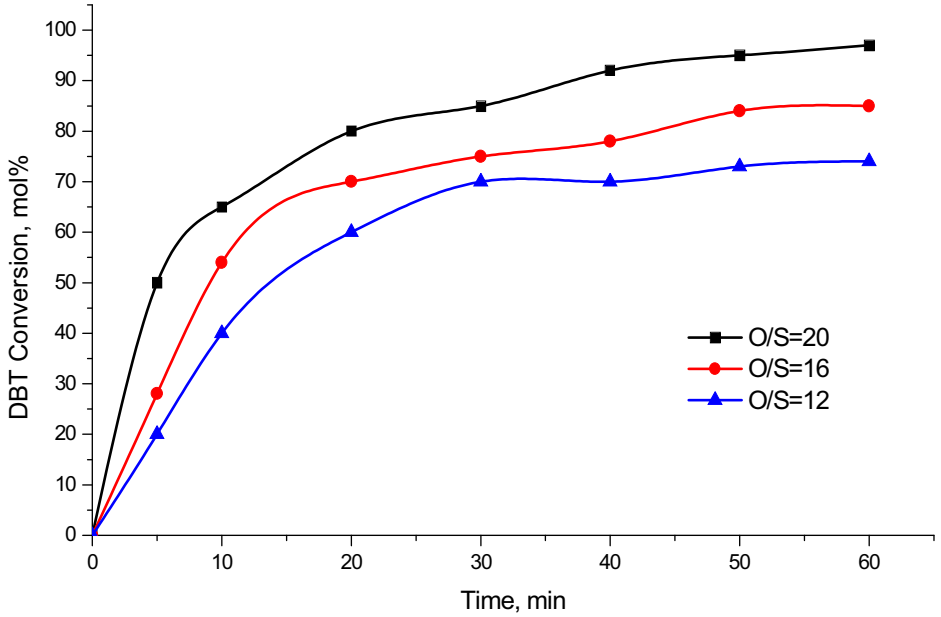


**Fig. 13.** Effect of the initial concentration of $H_2O_2$ over V-CMK-3(7%). T = 60 °C. g DBT/g cat = 4.8 (2000 ppm), in L–S phase system.

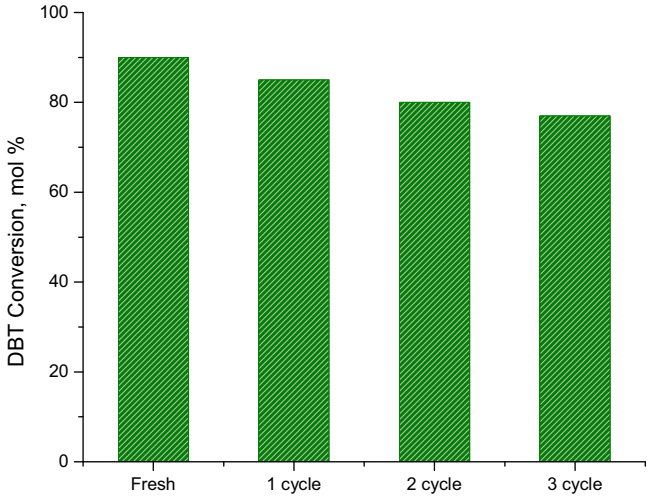


**Fig. 14.** Deactivation study of V-CMK-3 (7%) at 10 min of reaction time. Molar ratio $H_2O_2$/DBT = 6 (O/S = 12), T = 60 °C, g DBT/g cat = 1.2 (500 ppm), in L–S phase system.

### 3.2.1. *Deactivation of the catalyst*

The deactivation of a catalyst is very important for industrial point of view. The reusability of the catalyst for the ODS of DBT has been tested after washing several times with water-methanol solution. After washing, all oxidized products that could be adsorbed on the catalysts are eliminated. In Fig. 14 we observe that the activity of the used sample remains after the second recycle compared to a fresh catalyst. Only after the third recycle we observe 13% of loss in conversion. This indicates that the active sites were maintained during the reaction. The reusability of the catalyst indicates that V-CMK-3 is a potential catalyst for the ODS of dibenzothiophene.

## 4. Conclusions

The results leaded us to conclude that 7 wt.% loaded V-CMK-3 is the most active catalyst for ODS of DBT using hydrogen peroxide as oxidant and acetonitrile as solvent. Under identical test conditions V-CMK-3 is more active than the Ti-CMK-3 and besides leads to 99–100% selectivity for the sulfone. The effective promoter (CMK-3) has high surface area and high pore volume; however, surface area and pore volume alone could not explain the observed trends in performance of ODS but these qualities could affect the better anchorage of the catalytic species in the carbons framework reaching high active sites distribution and more stable metallic oxides nanoparticles.

## Acknowledgments

The authors are very grateful to Drs. J.L. García Fierro, J.M Martin for XPS and UV–vis-DRS characterization performed in ICP-CSIC. Madrid.

We thank CONICET Argentina, PIP CONICET 11220120100218CO (2013–2016), and MINCyTCba, 1210/07 (2014–2016) for financial assistance.

## References

[1] K.S. Triantafyllidis, E.A. Deliyanni, Chem. Eng. J. 236 (2014) 406–414.
[2] K. Kedra-Krolik, F. Mutelet, J.C. Moise, J.N. Jaubert, Energy Fuels 25 (2011) 1559–1565.
[3] D. Liu, J.Z. Gui, Z.L. Sun, J. Mol. Catal. A: Chem. 291 (2008) 17–21.
[4] X. Han, H. Lin, Y. Zheng, Sep. Purif. Technol. 133 (2014) 194–203.
[5] S.O. Ribeiro, D. Julião, L. Cunha-Silva, V.F. Domingues, R. Valença, J.C. Ribeiro, B. de Castro, S.S. Balula, Fuel 166 (2016) 268–275.
[6] V.C. Srivastava, RSC Adv. 2 (2012) 759–783.
[7] B. Pawelec, R.M. Navarro, J.M. Campos-Martin, J.L.G. Fierro, Catal. Sci. Technol. 1 (2011) 23–42.
[8] C. Song, Catal. Today 86 (2003) 211–263.
[9] S. Maghsoudi, A. Kheirolomoom, M. Vossoughi, E. Tanaka, S. Katoh, Biochem. Eng. J. 8 (2000) 151–156.
[10] X.L. Zhou, Q. Tan, G.X. Yu, L.F. Chen, J.A. Wang, O. Novaro, Kinet. Catal. 50 (4) (2009) 543–549.
[11] S. Haji, C. Erkey, Ind. Eng. Res. 42 (2003) 6933–6937.
[12] F. Subhan, B.S. Liu, Y. Zhang, X.G. Li, Fuel Process. Technol. 97 (2012) 71–78.
[13] M.C. Capel-Sanchez, P. Perez-Presas, J.M. Campos-Martin, J.L.P. Fierro, Catal. Today 157 (2010) 390–396.
[14] Y. Jia, G. Li, G. Ning, Fuel Process. Technol. 92 (2011) 106–111.
[15] S. Dhir, R. Uppaluri, M.K. Purkait, J. Hazard. Mater. 161 (2009) 1360–1368.
[16] H. Gomez-Bernal, L. Cedeño-Caero, A. Gutierrez-Alejandre, Catal. Today 142 (2009) 227–233.
[17] F.S. Mjalli, O.U. Ahmed, T. Al-Wahaibi, Y. Al-Wahaibi, I.M. Al Nashef, Rev. Chem. Eng. 30 (2014) 337–378.
[18] J.M. Campos-Martin, M.C. Capel-Sanchez, P. Perez-Presas, J.L.G. Fierro, J. Chem. Technol. Biotechnol. 85 (2010) 879–890.
[19] A. Chica, A. Corma, M.E. Dómine, J. Catal. 242 (2006) 299–308.
[20] L.P. Rivoira, V.A. Vallés, B.C. Ledesma, M.V. Ponte, M.L. Martínez, O.A. Anunziata, A.R. Beltramone, Catal. Today 271 (2016) 102–113.
[21] A.D. Giuseppe, M. Crucianelli, Appl. Catal. B-Environ. 89 (2009) 239–245.
[22] B. Wang, J. Zhu, H. Ma, J. Hazard. Mater. 164 (2009) 256–264.
[23] N.F. Nejad, E. Shams, M.K. Amini, Pet. Sci. Technol. 32 (2014) 1537–1544.
[24] E.B. Krivtsov, A.K. Golovko, Petrol Chem. 54 (2014) 51–57.
[25] E. Lissner, W.F. de Souza, B. Ferrera, J. Dupont, Chem. Sus. Chem. 2 (2009) 962–964.
[26] Y. Nie, Y.X. Dong, L. Bai, H.F. Dong, X.P. Zhang, Fuel 103 (2013) 997–1002.
[27] W. Jiang, W.S. Zhu, Y.H. Chang, H.M. Li, Y.H. Chao, J. Xiong, H. Liu, S. Yin, Energ. Fuel 28 (2014) 2754–2760.
[28] Y.X. Dong, Y. Nie, Q. Zhou, Chem. Eng. Technol. 36 (2013) 435–442.
[29] G.R. Yu, J.J. Zhao, D.D. Song, C. Asumana, X.Y. Zhang, X.C. Chen, Ind. Eng. Chem. Res. 50 (2011) 11690–11697.
[30] L.S. Nogueira, S. Ribeiro, C.M. Granadeiro, E. Pereira, G. Feio, L. Cunha-Silva, S.S. Balula, Dalton Trans. 43 (2014) 9518–9528.
[31] C.J. Zou, P.W. Zhao, J. Ge, Y.B. Qin, P.Y. Luo, Fuel 104 (2013) 635–640.
[32] K.G. Haw, W.A.W. Abu Bakar, R. Ali, J.F. Chong, A.A.A. Kadir, Fuel Process. Technol. 91 (2010) 1105–1112.
[33] M.T. Timko, E. Schmois, P. Patwardhan, Y. Kida, C.A. Class, W.H. Green, R.K. Nelson, C.M. Reddy, Energy Fuel 28 (2014) 2977–2983.
[34] M.T. Timko, J.A. Wang, J. Burgess, P. Kracke, L. Gonzalez, C. Jaye, D.A. Fischer, Fuel 163 (2016) 223–231.
[35] Y. Qiao, C. Miao, Y. Yue, Z. Xie, W. Yang, W. Hua, Z. Gao, Microporous Mesoporous Mater. 119 (2009) 150–157.
[36] L. Cedeño-Caero, M. Ramos-Luna, M. Mendez-Cruz, J. Ramirez-Solis, Catal. Today 172 (2011) 189–194.
[37] A.T. Shah, B.S. Li, Z.E.A. Abdalla, J. Colloid Interf. Sci. 336 (2009) 707–711.
[38] C.Z. Jin, G. Li, X.S. Wang, Y. Wang, L.X. Zhao, D.W. Sun, Microporous Mesoporous Mater. 111 (2008) 236–242.
[39] T.W. Kim, M.J. Kim, F. Kleitz, M.M. Nair, R. Guillet-Nicolas, K.E. Jeong, H.J. Chae, C.U. Kim, S.Y. Jeong, Chem. Cat. Chem. 4 (2012) 687–697.
[40] G. Rodriguez-Gattorno, A. Galano, E. Torres-Garcia, Appl. Catal. B-Environ. 92 (2009) 1–8.
[41] E. Torres-Garcia, A. Galano, G. Rodriguez-Gattorno, J. Catal. 282 (2011) 201–208.
[42] A. Akbari, M. Omidkhah, J.T. Darian, Ultrason. Sonochem. 21 (2014) 692–705.
[43] M. Teymouri, A. Samadi-Maybodi, A. Vahida, A. Miranbeigi, Fuel Process. Technol. 116 (2013) 257–264.
[44] N. Farzin Nejad, E. Shams, M.K. Amini, J.C. Bennett, Microporous Mesoporous Mater. 168 (2013) 239–246.
[45] Y. Shi, X. Zhang, G. Liu, Fuel 158 (2015) 565–571.
[46] J.M. Juárez, M.B. Gómez Costa, O.A. Anunziata, Int. J. Energy Res. 39 (2015) 128–139.
[47] H. Yang, D. Zhao, J. Mater. Chem. 15 (2005) 1217–1231.
[48] H. Huwe, M. Fröba, Microporous Mesoporous Mater. 60 (2003) 151–158.
[49] U. Suryavanshia, T. Iijima, A. Hayashia, Y. Hayashia, M. Tanemura, Chem. Eng. J. 179 (2012) 388–393.
[50] V.I. Khitrova, M.F. Bundule, Z.G. Pinsker, Kristallografiya 22 (1977) 1253, Calculated from ICSD using POWD-12++, (1997).
[51] M.B. Gómez Costa, J.M. Juárez, M.L. Martínez, A.R. Beltramone, J. Cussa, O.A. Anunziata, Mater. Res. Bull. 48 (2013) 661–667.
[52] E. Veena Gopalan, K.A. Malini, G. Santhoshkumar, T.N. Narayanan, P.A. Joy, I.A. Al-Omari, D. Sakthi Kumar, Y. Yoshida, M.R. Anantharaman, Nanoscale Res. Lett. 5 (2010) 889–897.
[53] S. Balaji, Y. Djaoued, J. Robichaud, J. Raman Spectrosc. 37 (2006) 1416–1422.
[54] M.S. Dresselhaus, A. Jorio, M. Hofmann, G. Dresselhaus, R. Saito, Nano Lett. 10 (2010) 751–758.
[55] W. Zhang, J. Cui, C. Tao, Y. Wu, Z. Li, L. Ma, Y. Wen, G. Li, Angew. Chem. 121 (2009) 5978–5982.
[56] F. Tuinstra, J.L. Koenig, J. Chem. Phys. 53 (1970) 1126.
[57] H. Darmstadt, C. Roy, S. Kaliaguine, S.J. Choi, R. Ryoo, Carbon 40 (2002) 2673–2683.
[58] J.C. Dupin, D. Gonbeau, P. Vinatier, A. Levasseur, Phys. Chem. Chem. Phys. 2 (2000) 1319–1324.
[59] J. Fang, X. Bi, D. Si, Z. Jiang, W. Huang, Appl. Surf. Sci. 253 (2007) 8952–8961.

[60] M.D. Soriano, J.A. Cecilia, A. Natoli, J. Jiménez, J.M. López Nieto, E. Rodríguez-Castellón, Catal. Today 254 (2015) 36–42.
[61] V.V. Atuchin, V.G. Kesler, N.V. Pervukhina, Z. Zhang, J. Electron. Spectrosc. Relat. Phenom. 152 (12) (2006) 18–24.
[62] G. Petrini, A. Cesana, G.F. De Alberti, G. Genoni, M. Leofanti, M. Padovan, G. Paparatto, P. Roffia, Stud. Surf. Sci. Catal. 68 (1991) 761–766.
[63] Z. Luan, E.M. Maes, P.A.W. Van der Heide, D. Zhao, R.S. Czernuszewicz, L. Kevan, Chem. Mater. 11 (1999) 3680–3686.
[64] S. Balaji, Y. Djaoued, J. Robichaud, J. Raman Spectrosc. 37 (2006) 1416–1422.
[65] A. Khodakov, J. Yang, S. Su, E. Iglesia, A.T. Bell, J. Catal. 177 (1998) 343–351.
[66] A. Khodakov, B. Olthof, A.T. Bell, E. Iglesia, J. Catal. 181 (1999) 205–216.
[67] M.A. Larrubia, G. Busca, Mater. Chem. Phys. 72 (2001) 337–346.
[68] J.G. Eon, R. Olier, J.C. Volta, J. Catal. 145 (1994) 318–326.
[69] P. Concepción, M.T. Navarro, T. Blasco, J.M. López Nieto, B. Panzacchi, F. Rey, Catal. Today 96 (2004) 179–186.
[70] G. Catana, R. Ramachandra Rao, B.M. Weckhuysen, P. Van Der Voort, E. Vansant, R.A. Schoonheydt, J. Phys. Chem. B 102 (1998) 8005–8012.
[71] B. Solsona, T. Blasco, J.M.L. Nieto, M.L. Peña, F. Rey, A. Vidal-Moya, J. Catal. 203 (2001) 443–452.
[72] D. Wei, H. Wang, X. Feng, W.T. Chueh, P. Ravikovitch, M. Lyubovsky, C. Li, T. Takeguchi, G.L. Haller, J. Phys. Chem. B 103 (1999) 2113–2121.
[73] M. Baltes, K. Cassiers, P. Van der Voort, B.M. Weckhuysen, R.A. Schoonheydt, E.F. Vansant, J. Catal. 197 (2001) 160–171.
[74] K. Chen, E. Iglesia, A.T. Bell, J. Catal. 192 (2000) 197–203.
[75] J.L. Male, H.G. Niessen, A.T. Bell, T.D. Tilley, J. Catal. 194 (2000) 431–444.
[76] S. Chen, Z. Qin, X. Xu, J. Wang, Appl. Catal. A-Gen. 302 (2006) 185–192.
[77] F. Arena, F. Frusteri, A. Parmaliana, Appl. Catal. A-Gen. 176 (1999) 189–199.
[78] J. Santamaría-González, J. Luque-Zambrana, J. Mérida-Robles, P. Maireles-Torres, E. Rodríguez-Castellón, A. Jiménez-López, Catal. Lett. 68 (2000) 67–73.
[79] M.S. Park, V.P. Vislovskiy, J.S. Chang, Y.G. Shul, J.S. Yoo, S.E. Park, Catal. Today 87 (2003) 205–212.
[80] H. Dai, A.T. Bell, E. Iglesia, J. Catal. 221 (2004) 491–499.
[81] B. Solsona, J.M.L. Nieto, U. Díaz, Microporous Mesoporous Mater. 94 (2006) 339–347.
[82] K.-S. Cho, Y.-K. Lee, Appl. Catal. B: Environ. 147 (2014) 35–42.
[83] D. Huang, Y.J. Wang, Y.C. Cui, G.S. Luo, Microporous Mesoporous Mater. 116 (2008) 378–385.
[84] E. Rafiee, S. Eavani, J. Mol. Catal. A: Chem. 380 (2013) 18–27.
[85] V. Hulea, F. Fajula, J. Bousquet, J. Catal. 195 (2001) 179–186.
[86] D. Wang, E.W. Qian, H. Amano, K. Okata, A. Ishihara, T. Kabe, Appl. Catal. A-Gen. 253 (2003) 91–99.
[87] A. Chica, A. Corma, M.E. Domine, J. Catal. 242 (2006) 299–308.
[88] O. Gonzalez-Garcia, L. Cedeño-Caero, Catal. Today 150 (2010) 237–243.
[89] O. Gonzalez-Garcia, L. Cedeño-Caero, Catal. Today 148 (2009) 42–48.
[90] L. Cedeño-Caero, H. Gomez-Bernal, A. Fraustro-Cuevas, H. Guerra-Gomez, R. Cuevas-Garcia, Catal. Today 133–135 (2008) 244–254.